Nanoscale

PAPER

View Article Online
View Journal | View Issue

Cite this: *Nanoscale*, 2015, **7**, 16781

Sodium-ion storage properties of nickel sulfide hollow nanospheres/reduced graphene oxide composite powders prepared by a spray drying process and the nanoscale Kirkendall effect†

G. D. Park, J. S. Cho and Y. C. Kang*

Received 26th June 2015,
Accepted 29th August 2015

DOI: 10.1039/c5nr04252f

www.rsc.org/nanoscale

Spray-drying and the nanoscale Kirkendall diffusion process are used to prepare nickel sulfide hollow nanospheres/reduced graphene oxide (rGO) composite powders with excellent Na-ion storage properties. Metallic Ni nanopowder-decorated rGO powders, formed as intermediate products, are transformed into composite powders of nickel sulfide hollow nanospheres/rGO with mixed crystal structures of Ni_3S_2 and Ni_9S_8 phases by the sulfidation process under H_2S gas. Nickel sulfide/rGO composite powders with the main crystal structure of Ni_3S_2 are also prepared as comparison samples by the direct sulfidation of nickel acetate–graphene oxide (GO) composite powders obtained by spray-drying. In electrochemical properties, the discharge capacities at the 150th cycle of the nickel sulfide/rGO composite powders prepared by sulfidation of the Ni/rGO composite and nickel acetate/GO composite powders at a current density of 0.3 A g^{-1} are 449 and 363 mA h g^{-1}, respectively; their capacity retentions, calculated from the tenth cycle, are 100 and 87%. The nickel sulfide hollow nanospheres/rGO composite powders possess structural stability over repeated Na-ion insertion and extraction processes, and also show excellent rate performance for Na-ion storage.

Introduction

Na-ion batteries (NIBs) have recently attracted much interest as potential large-scale energy storage systems, because of the low cost associated with the high natural abundance of Na.[1–7] However, efficient electrode materials must be developed before NIBs are commercialized. The electrode materials must be capable of overcoming the slow Na-ion diffusion kinetics and resisting structural pulverization during charge/discharge, which often occurs owing to the large ionic radius of Na.[8–10] The exploration of anode materials for NIBs has focused on materials commonly used as anodes for Li-ion batteries (LIBs), including carbon-based materials.[11–14] These showed large initial capacity losses and low reversible capacities for Na-ion storage. Transition metal oxides, which exhibited good Li-ion storage performances, did not have satisfactory Na-ion storage performances, despite their excellent electrochemical properties in LIBs. Recently, non-oxide materials, such as sulfides, selenides, and phosphides, have shown good Na-ion storage properties as anode materials for NIBs.[15–29] The Na-ion storage properties of these non-oxide materials were further improved by their integration with carbon-based materials, which enhances the anode's electrical conductivity and structural stability during cycling.[24–29]

The combination of nanostructured non-oxide materials and carbon-based materials is considered an effective method for developing efficient NIB anode materials. In particular, graphene has superior electrical conductivity and high mechanical strength compared to other carbon-based materials.[30–38] Nanostructured non-oxide material/graphene composites have displayed good Na-ion storage performances.[24–27] In recent years, the application of nanoscale Kirkendall diffusion for producing hollow nanospheres has been successfully implemented to create nanostructured metal oxide/graphene composites that exhibit excellent Li-ion storage properties.[39–42] In addition, hollow metal sulfide nanospheres have been successfully prepared using the nanoscale Kirkendall diffusion process.[43–46] The difference between the rates of the outward diffusion of metal cations through the sulfide layer and the inward diffusion of sulfur ions into the metals during the sulfidation process creates metal sulfide hollow nanopowder. However, to the best of our knowledge, the nanoscale

Department of Materials Science and Engineering, Korea University, Anam-Dong, Seongbuk-Gu, Seoul 136-713, Republic of Korea. E-mail: yckang@korea.ac.kr; Fax: (+82) 2-928-3584

†Electronic supplementary information (ESI) available. See DOI: 10.1039/c5nr04252f

Kirkendall diffusion process has not been applied in the preparation of nanostructured metal sulfide (or other non-oxide materials)/graphene composites for use in NIBs.

In this study, composite powders of nickel sulfide hollow nanospheres/reduced graphene oxide (rGO) were prepared by spray-drying with the application of the nanoscale Kirkendall diffusion process. Crumpled rGO sheets, uniformly decorated with nickel sulfide hollow nanospheres, were prepared by a two-step post-treatment of the precursor powders obtained by a large-scale spray-drying process. Metallic Ni nanopowder-decorated rGO powders were prepared as intermediate products by post-treatment under a reducing atmosphere of spray-dried powders consisting of nickel acetate and graphene oxide (GO). The transformation of the Ni nanopowders into hollow nanospheres of nickel sulfide by inducing the nanoscale Kirkendall diffusion process with post-treatment under H_2S gas resulted in nickel sulfide hollow nanospheres/rGO composite powders. The Na-ion storage properties of the nickel sulfide hollow nanospheres/rGO composite powders were compared with those of the nickel sulfide dense nanospheres/rGO composite powders, in which the nanoscale Kirkendall diffusion process did not occur.

Experimental section

Sample preparation

A three-step process was used for the preparation of the nickel sulfide hollow nanospheres/rGO composite powders. Nickel acetate/GO precursor powders were prepared directly by a simple spray-drying process using a spray solution of nickel acetate tetrahydrate ($Ni(CH_3COO)_2{\cdot}4H_2O$) and GO nanosheets. The GO nanosheets were synthesized from graphite flakes using a modified Hummers method. The as-synthesized GO nanosheets were re-dispersed in distilled water and then exfoliated by ultrasonication. 0.1 M of $Ni(CH_3COO)_2{\cdot}4H_2O$ was dissolved in 500 mL distilled water with 2 mg mL^{-1} dispersed exfoliated GO to fabricate the nickel acetate/GO precursor. In the spray-drying process, a colloidal liquid containing GO nanosheets was pumped to an atomizing device, where it was transformed into a spray of small droplets. These droplets met a stream of hot air for drying. The resulting dry powder was separated from the humid air by the centrifugal forces in a cyclone system. The temperatures at the inlet and outlet of the spray dryer were 300 °C and 125 °C, respectively. A two-fluid nozzle was used as the atomizer with an atomization pressure of 0.5 bar. In the first step of the post-treatment process, the precursor powders obtained by spray-drying were treated in a 10% H_2/Ar reducing atmosphere at a temperature of 300 °C for 10 h to form metallic Ni/rGO composite powders. In the second step of the post-treatment process, an alumina boat containing these Ni/rGO composite powders was loaded into a larger, covered alumina boat. Thiourea powders were loaded on the outside of the small alumina boat as the sulfur source for the sulfidation of the Ni/rGO composite powders. The Ni/rGO composite powders were sulfidized at 300 °C for 12 h in the presence of a 10% H_2/Ar reducing gas, resulting in nickel sulfide hollow nanospheres/rGO composite powders by the nanoscale Kirkendall diffusion process. To fabricate the nickel sulfide dense nanospheres/rGO composite powders, the nickel acetate/GO precursor powders directly prepared by spray-drying were sulfidized at 300 °C for 12 h in the presence of 10% H_2/Ar gas.

Characterization

The crystal structures of the powders were investigated using X-ray diffractometry (XRD, X'pert PRO MPD) with Cu-K_α radiation (λ = 1.5418 Å) at the Korea Basic Science Institute (Daegu). The morphologies of the powders were investigated using field-emission scanning electron microscopy (FE-SEM, Hitachi S-4800) and high-resolution transmission electron microscopy (HR-TEM, JEOL JEM-2100F) at a working voltage of 200 kV. The specific surface areas of the powders both before and after post-treatment at various temperatures were calculated by the Brunauer–Emmett–Teller (BET) analysis of N_2 adsorption measurements (TriStar 3000). X-ray photoelectron spectroscopy (XPS) spectra of the powders were obtained using ESCALAB-250 with Al Kα radiation (1486.6 eV). To determine the amount of rGO in the nickel sulfide hollow nanospheres/rGO composite powders, thermogravimetric analysis (TGA, SDT Q600) was performed in air at a heating rate of 10 °C min^{-1}.

Electrochemical measurements

The electrochemical properties of the fabricated powders were analyzed by constructing a 2032-type coin cell. The anode was prepared by mixing the active material, carbon black, and sodium carboxymethyl cellulose (CMC) in a weight ratio of 70 : 20 : 10. Na metal and microporous polypropylene film were used as the counter electrode and the separator, respectively. The electrolyte was 1 M $NaClO_4$ (Aldrich) dissolved in a mixture of ethylene carbonate/dimethyl carbonate (EC/DMC; 1 : 1 v/v), to which 5 wt% fluoroethylene carbonate (FEC) was added. The discharge/charge characteristics of the samples were investigated by cycling the cells in the 0.001–3 V potential range at various current densities. Cyclic voltammograms (CV) were measured at a scan rate of 0.1 mV s^{-1}. The dimensions of the anode were 1 cm × 1 cm and the mass loading was approximately 1.2 mg cm^{-2}. The electrochemical impedance was measured using electrochemical impedance spectroscopy (EIS) over the frequency range of 0.01 Hz–100 kHz.

Results and discussion

The formation mechanism of the crumpled rGO powder uniformly decorated with nickel sulfide hollow nanospheres is described in Scheme 1 and Fig. S1.† The nickel acetate/GO composite powder with this crumpled structure was prepared by a spray drying process. The first step of the post-treatment of the composite powder under a reducing atmosphere produced the crumpled rGO powder uniformly decorated with

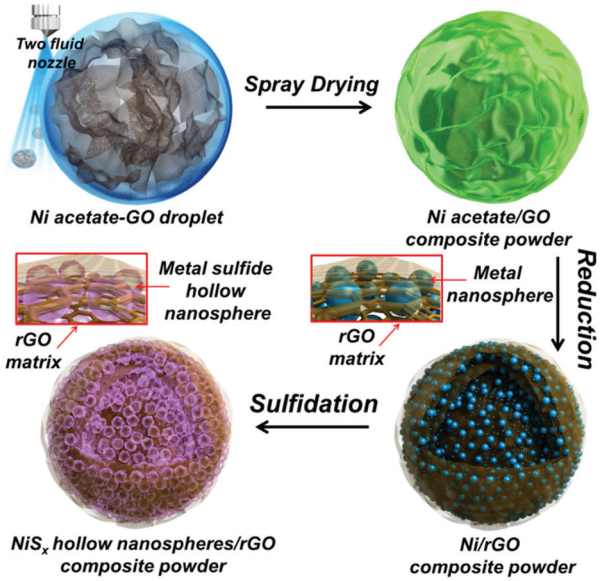

Scheme 1 Formation mechanism of the nickel sulfide hollow nanospheres–rGO composite powder by nanoscale Kirkendall diffusion.

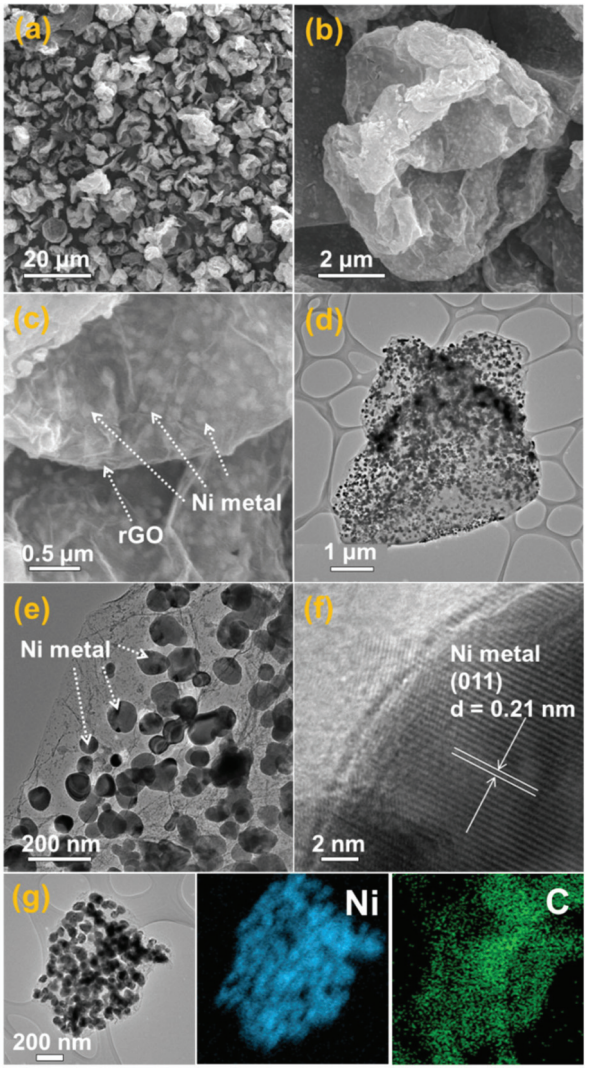

Fig. 1 Morphologies and elemental mapping images of Ni nanopowders/rGO composite powders: (a), (b) and (c) SEM images, (d) and (e) TEM images, (f) HR-TEM image, and (g) elemental mapping images.

solid Ni nanopowders. These Ni nanopowders were transformed into hollow nanospheres of nickel sulfide by the nanoscale Kirkendall effect through sulfidation under an atmosphere of H_2S.

The precursor powders for the nickel sulfide hollow nanospheres/rGO composite powders were prepared by a spray drying process from a colloidal spray solution of GO nanosheets and nickel acetate. The decomposition of nickel acetate and the thermal reduction of GO into rGO did not occur during the spray drying process. The evaporation of water allowed the temperature of each droplet during spray drying to remain lower than the spray dryer's inlet temperature. Therefore, the precursor powders prepared by the spray drying process were composite of nickel acetate/GO. The SEM images shown in Fig. S2† show the crumpled structure of the nickel acetate/GO precursor powders prepared directly by a spray drying process. One crumpled composite powder particle was formed from each droplet by drying. The complete drying of the droplets resulted in the formation of an aggregation-free powder of the nickel acetate/GO composite. The GO nanosheets enhanced the stability of nickel acetate under high humidity. The crumpled powders contain high-thickness walls, as shown by arrows in Fig. S2d.†

The reduction of the nickel acetate/GO composite powders at 300 °C for 10 h under H_2/Ar gas produced Ni/rGO composite powders. Both decomposition and reduction of nickel acetate into Ni through the reaction intermediate NiO occur during this process, as confirmed by the XRD pattern shown in Fig. S3.† The thermal reduction of the GO nanosheets into rGO nanosheets also occurs at this point. The crumpled structure of the precursor powders is maintained after reduction, as shown in SEM images in Fig. 1a and b. The high-resolution SEM image shown in Fig. 1c reveals uniformly dispersed Ni nanopowders covered with rGO nanosheets. The TEM images in Fig. 1d and e show Ni nanopowders of several tens of nanometers in size uniformly dispersed over a matrix of rGO. Ultrafine nanopowders of several nanometers in size surround the Ni nanoparticles of several tens of nanometers in size, as observed in the high-resolution TEM image in Fig. 1e. The high-resolution TEM image shown in Fig. 1f shows clear lattice fringes separated by 0.21 nm, which corresponds to the (011) crystal plane of metallic Ni. The segregation and crystal growth of metallic Ni during the long-term reduction process resulted in Ni nanoparticles, which became uniformly dispersed over the rGO matrix. The rGO nanosheets acted as protection layers for the Ni particle growth at low sintering temperatures, resulting in aggregation-free Ni nanopowders of several tens of nanometers in size. The captured

metallic Ni on the rGO nanosheets resulted in ultrafine Ni nanocrystals. The elemental mapping images shown in Fig. 1g show the uniform distribution of Ni nanopowders throughout the rGO matrix.

The sulfidation of Ni/rGO composite powders at 300 °C for 12 h under H_2S gas, formed by the decomposition of thiourea, produced nickel sulfide/rGO composite powders. Similar nickel sulfide/rGO composite powders were also formed from the nickel acetate/GO composite powders obtained directly by a spray drying process. The XRD patterns shown in Fig. S3† show the complete sulfidation of the Ni/rGO composite and nickel acetate/GO composite powders to form nickel sulfide/rGO composite powders. The powders formed from the nickel acetate/GO composite have a main crystal structure of Ni_3S_2, with minor peaks corresponding to Ni_9S_8. However, the powders formed from the Ni/GO composite powders show crystal structures mixing Ni_3S_2 and Ni_9S_8 phases. The mean crystallite sizes of the nickel sulfide/rGO composite prepared from the Ni/rGO composite and the nickel acetate/GO composite, calculated from the XRD peak widths of the Ni_3S_2 phase using the Scherrer equation, were 25 and 45 nm, respectively. The broad XRD peak located near 25° could be attributed to the rGO layers. The thermogravimetric (TG) curve of the nickel sulfide hollow nanospheres/rGO composite powders is shown in Fig. S4.† The TG curve exhibits several steps of weight loss due to the evaporation of adsorbed water molecules at temperatures below 200 °C, the oxidation of nickel sulfide to NiO, and the combustion of rGO. The rGO content of the nickel sulfide hollow nanospheres/rGO composite powders was estimated as 23 wt%. The BET surface areas of the nickel sulfide/rGO composite powders prepared by the sulfidation of the Ni/rGO and the nickel acetate/GO composites were 26 and 37 $m^2\ g^{-1}$, respectively.

The morphologies of the nickel sulfide/rGO composite powders prepared from Ni/rGO are shown in Fig. 2. The SEM images shown in Fig. 2a and b reveal a similarity in morphology between the nickel sulfide/rGO composite and the Ni/rGO composite. However, the TEM images shown in Fig. 2c and d display the unique structure of the nickel sulfide/rGO composite powders. The hollow nanospheres of nickel sulfide are seen to be uniformly distributed across the rGO matrix. The solid Ni nanopowders are shown to have been transformed into hollow nanospheres of nickel sulfide by the well-known nanoscale Kirkendall effect through sulfidation under H_2S gas. In the early stages of sulfidation, a Ni@nickel sulfide core@shell nanopowder was formed by the surface sulfidation of the Ni nanopowder. Ni cations with small radii (83 pm) diffused outward more quickly than the larger sulfur anions (170 pm) which diffused inward, forming Ni@nickel sulfide nanopowders with internal voids. The voids inside the nanopowder particles, formed by nanoscale Kirkendall diffusion, increased in size with increasing sulfidation time. Finally, the nickel sulfide hollow nanosphere resulted. The low melting temperature of nickel sulfide deforms the completely hollow spheres formed by nanoscale Kirkendall diffusion into broken hollow spheres, as shown by arrows in the TEM images. The

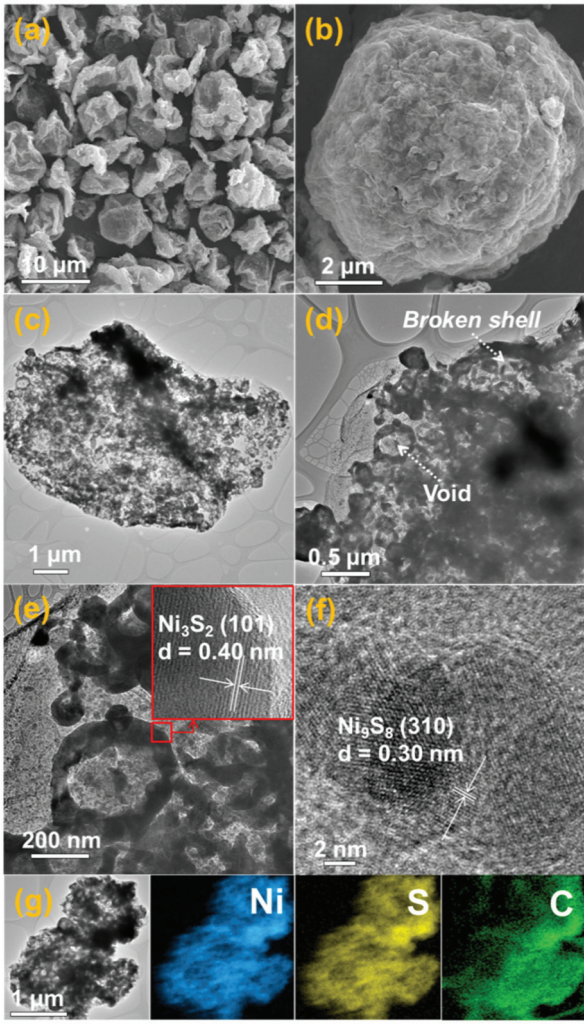

Fig. 2 Morphologies and elemental mapping images of nickel sulfide hollow nanospheres/rGO composite powders obtained by nanoscale Kirkendall diffusion: (a) and (b) SEM images, (c) and (d) TEM images, (e) and (f) HR-TEM image, and (g) elemental mapping images.

high-resolution TEM image shown in Fig. 2e displays clear lattice fringes separated by 0.4 nm, corresponding to the (101) crystal plane of Ni_3S_2. The high-resolution TEM image of the nanocrystals dispersed around the hollow nanospheres shows clear lattice fringes separated by 0.3 nm, corresponding to the (310) crystal plane of Ni_9S_8, as shown in Fig. 2f. Elemental mapping images, shown in Fig. 2e, display the uniform distribution of hollow nanospheres of nickel sulfide across the entire crumpled rGO matrix. Consequently, crumpled rGO powders decorated with deformed hollow nanospheres of nickel sulfide were successfully prepared by this two-step post-treatment processing of the spray-dried precursor.

The morphologies of the Ni_3S_2/rGO composite powders with a minor phase of Ni_9S_8, prepared by the direct sulfidation of nickel acetate/GO composites, are shown in Fig. 3. The SEM images shown in Fig. 3a and b show the similarity in morphology with the nickel sulfide/rGO composite powders pre-

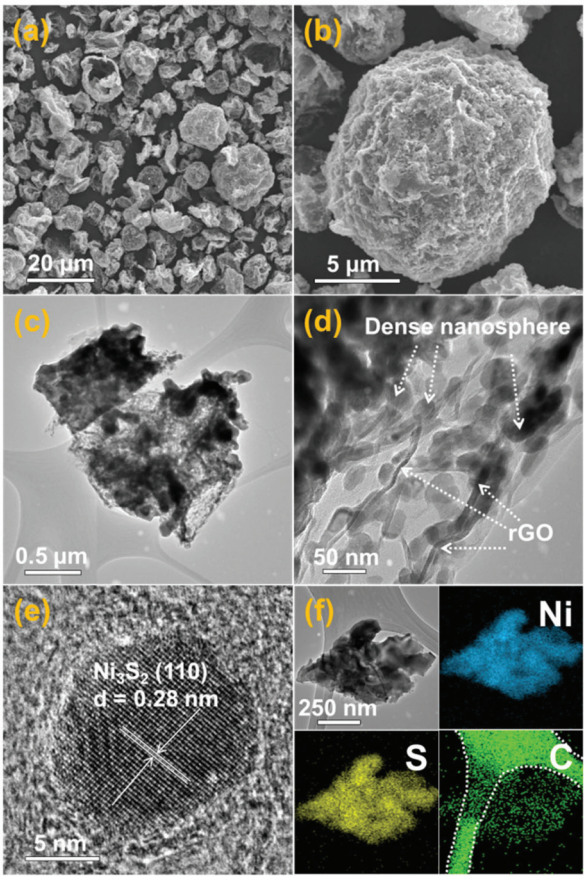

Fig. 3 Morphologies and elemental mapping images of nickel sulfide dense nanospheres/rGO composite powders obtained by direct sulfidation of nickel acetate/GO composite: (a) and (b) SEM images, (c) and (d) TEM images, (e) HR-TEM image, and (f) elemental mapping images.

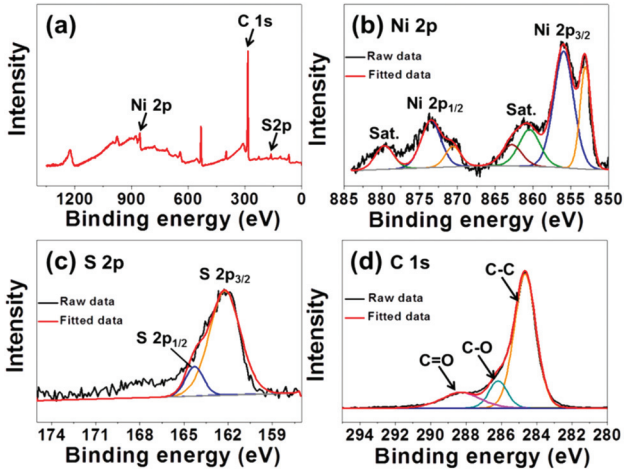

Fig. 4 XPS spectra of the nickel sulfide hollow nanospheres/rGO composite powders: (a) wide-scan XPS spectrum, (b) Ni 2p, (c) S 2p, and (d) C 1s.

pared by the direct sulfidation of Ni/rGO. However, the TEM images shown in Fig. 3c and d display the irregularity in the morphologies of the Ni_3S_2/rGO composite powders. Ni_3S_2 nanopowders have irregular shapes and a broad size distribution, distributed randomly over the rGO matrix. The high-resolution TEM image in Fig. 3e shows clear lattice fringes separated by 0.28 nm, which corresponds to the (110) crystal plane of Ni_3S_2. Elemental mapping images, shown in Fig. 3f, display the distribution of dense nanospheres of nickel sulfide across the entire crumpled rGO matrix.

The chemical state and molecular environment of the nickel sulfide/rGO composite powders prepared by the sulfidation of Ni/rGO were characterized by X-ray photoelectron spectroscopy (XPS). The XPS survey spectrum in Fig. 4a of the as-obtained nickel sulfide/rGO confirms the presence of Ni, S, and C signals. In the Ni 2p spectrum of the nickel sulfide/rGO composite, shown in Fig. 4b, the main peaks observed occur at binding energies of 855.9 eV for Ni $2p_{3/2}$ and 873.4 eV for Ni $2p_{1/2}$; these are characteristic of Ni_3S_2 and two shake-up satellites.[47,48] The valence states of nickel ions in Ni_3S_2 are mostly Ni^+ and partial Ni^{2+}. Therefore, the Ni $2p_{3/2}$ line surprisingly appears at 853.1 eV indicating the presence of divalent Ni species. In the S 2p spectrum of the nickel sulfide/rGO composite, shown in Fig. 4c, the spectrum shows the core-level band of the S 2p region, with peaks at 164.3 and 162.2 eV corresponding to S $2p_{1/2}$ and S $2p_{3/2}$, respectively.[49,50] Fig. 4d shows the C 1s XPS spectrum of the nickel sulfide/rGO composite powders. The C 1s peak of pure graphene oxide (GO) in the XPS profile shows peaks corresponding to sp^2 bonded carbon (C–C), epoxy and alkoxy groups (C–O), and carbonyl and carboxylic (C═O) components at 284.6, 286.6, and 288.1 eV, respectively.[51] The C–C bond peak is strong, while the C–O and C═O peaks are weak. This indicates the thermal reduction of GO nanosheets to rGO nanosheets during the preparation process of the nickel sulfide/rGO composite.

The electrochemical properties of the nickel sulfide/rGO composite powders prepared by the sulfidation of Ni/rGO powders for Na-ion storage performance were compared with those of the Ni_3S_2/rGO composite powders prepared by the direct sulfidation of nickel acetate/GO composite powders. The results are shown in Fig. 5. The CV curves of the two samples for the first five cycles are shown in Fig. 5a and b. The two nickel sulfide/rGO composite powders have similar shapes in their initial discharge and charge curves. The main reduction peak at approximately 0.6 V and the minor reduction peak at approximately 1.0 V are observed in the first discharge curves of both materials. The first peak could be attributed to the transformation of Ni_9S_8 to Ni_3S_2 at a higher potential of approximately 1.0 V; the second peak could be attributed to the conversion of Ni_3S_2 to metallic Ni and Na_2S at a lower potential of approximately 0.6 V by the following equation: $4Na^+ + 4e^- + Ni_3S_2 \rightarrow 3Ni + 2Na_2S$.[27] The two nickel sulfide/rGO composite powders have similar oxidation peaks in their first charge curves. The minor oxidation peak at approximately 1.3 V and the major oxidation peak at approximately 1.6 V could be attributed to the continuous oxidation of Ni to Ni^+

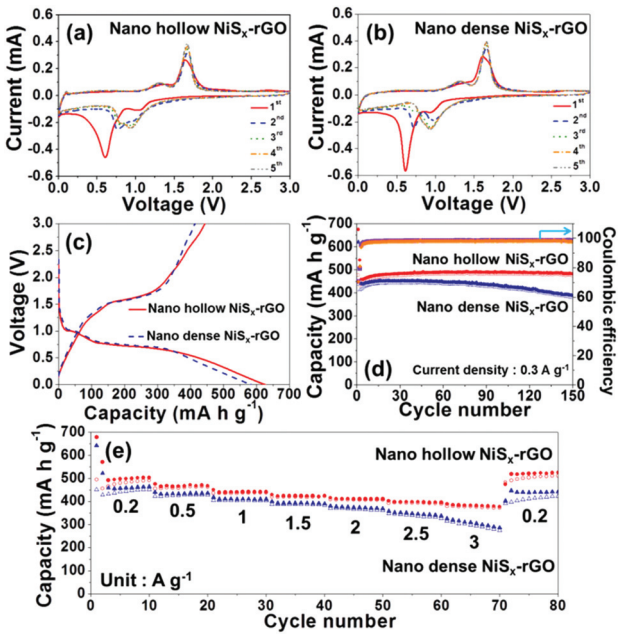

Fig. 5 Electrochemical properties of the nickel sulfide hollow and dense nanospheres/rGO composite powders: (a) and (b) CV curves, (c) initial charge–discharge curves, (d) cycling performances and Coulombic efficiencies, and (e) rate performances.

and the partial oxidation of Ni^{+} to Ni^{2+}, respectively. During the first two cycles, the reduction peaks of both nickel sulfide/rGO composite powders shift to higher voltages due to the electrode's improved kinetics by the formation of ultrafine nanoclusters. The well-overlapped CV curves from the third cycle indicate the good cycling stability of both nickel sulfide/rGO composite powders for Na-ion storage.

The initial discharge and charge curves at a current density of 0.3 A g^{-1} of the two composite powders are shown in Fig. 5c. The two plateaus observed at approximately 1.0 and 0.7 V in the initial discharge curves coincide well with the peaks in the CV results shown in Fig. 5a. Clear plateaus are not observed in the discharge curve of the second cycle, likely due to the transformation of crystalline nanoparticles into ultrafine nanocrystals during the first cycle. The initial discharge capacities of the nickel sulfide/rGO composite powders prepared from the Ni/rGO composite and the nickel acetate/GO composite are 626 and 584 mA h g^{-1}, respectively; their corresponding initial charge capacities are 443 and 413 mA h g^{-1}. The initial Coulombic efficiencies of the electrodes containing materials prepared by sulfidation of the Ni/rGO composite and the nickel acetate/GO composite were 71 and 71%, respectively; their Coulombic efficiencies for the second cycles were 80 and 81%. The large irreversible capacity losses in their second cycles and the second discharge capacities exceeding their initial charge capacities reveal the partial activation of nickel sulfide during both electrodes' first cycles. The cycling performances and Coulombic efficiencies of the two composite powders at a current density of 0.3 A g^{-1} are shown in Fig. 5d. The discharge capacities and Coulombic efficiencies of the two composite powders increase from the 3rd to the 10th cycle, due to the gradual activation of nickel sulfide during repeated cycling. The nickel sulfide/rGO active material, prepared from the Ni/rGO composite powders, maintains its high discharge capacity during the subsequent 140 cycles. However, the discharge capacity of the nickel sulfide/rGO composite active material, prepared by the sulfidation of the nickel acetate/GO composite powders, decreases gradually during the same period. The discharge capacities at the 150th cycle of the electrodes containing active materials prepared by the sulfidation of the Ni/rGO composite and nickel acetate/GO composite powders are 449 and 363 mA h g^{-1}, respectively; their capacity retentions, calculated from the tenth cycle onward, were 100 and 87%. The rate performance of the nickel sulfide/rGO active material prepared by the sulfidation of the Ni/rGO composite is shown in Fig. 5e, in which the current density is increased step-wise from 0.2 to 3 A g^{-1}. The electrode has final discharge capacities of 504, 468, 442, 426, 411, 395, and 377 mA h g^{-1} at current densities of 0.2, 0.5, 1, 1.5, 2, 2.5, and 3 A g^{-1}, respectively. The discharge capacity of the composite powders recovers well when the current density is returned to 0.2 A g^{-1} after cycling at high current densities. EIS of the two types of nickel sulfide/rGO composite powders was conducted to confirm their different Na-ion storage properties. The impedance measurements of the composite powders were per-

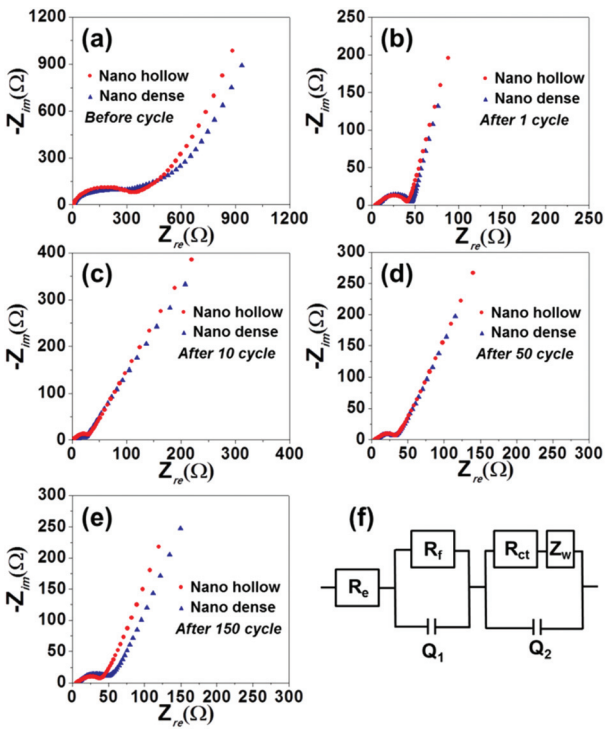

Fig. 6 Nyquist plots of the nickel sulfide hollow and dense nanospheres/rGO composite powders: (a) before cycling, (b) after 1st cycle, (c) after 10th cycle, (d) after 50th cycle, (e) after 150th cycle, and (f) equivalent circuit model used for ac impedance fitting.

formed at room temperature before and after 1, 10, 50, and 100 cycles at a current density of 1 A g^{-1}. The Nyquist plots shown in Fig. 6 reveal semicircles in the medium-frequency range, assigned to the charge-transfer resistance (R_{ct}) of the electrodes.[52] The two types of nickel sulfide/rGO composite powders have similar R_{ct} before cycling. The R_{ct} of the two composite powders decreases abruptly after the first cycle, due to the transformation of the crystalline nickel sulfide to ultrafine nanocrystals during the first cycle. The R_{ct} of the two types of composite powders obtained after the 10^{th} cycle is lower than those of the powders obtained after the first cycles owing to the gradual activation of nickel sulfide during the first 10 cycles. The R_{ct} values of the nickel sulfide/rGO composite powders prepared by the sulfidation of the Ni/rGO composite powders after 50 and 150 cycles (Fig. 6d and e) are 40 and 46 Ω, respectively. However, the R_{ct} values of the composite powders prepared by the sulfidation of the nickel acetate/GO composite powders after 50 and 150 cycles (Fig. 6d and e) are 37 and 61 Ω, respectively. The structural stability of the nickel sulfide hollow nanospheres/rGO composite powders prepared by the nanoscale Kirkendall diffusion process is maintained during the repeated Na insertion and extraction processes; the powders also maintain their low R_{ct} during cycling. Therefore, the structural stability of the nickel sulfide hollow nanospheres/rGO composite powders is correlated to their excellent Na-ion storage properties.

The three-dimensional (3D) porous MoS_2–rGO and WS_2–rGO composite powders prepared by spray pyrolysis showed outstanding Na-ion storage properties as anode materials for NIBs.[24,25] However, the 3D porous structure formed by decomposition of polystyrene (PS) nanobeads reduces the volumetric capacities of the composite powders. However, the formation of ultrafine hollow nickel sulfide nanospheres by the nanoscale Kirkendall diffusion process will slightly change the volumetric capacities of the nickel sulfide–rGO composite powders. In addition, the single component nickel sulfide–rGO composite powders with unique structures showed comparable Na-ion storage properties to those of the multicomponent $Ni_3Co_6S_8$–rGO composite powders.[26]

Conclusions

Metal sulfide hollow nanospheres/rGO composite powders were prepared by a spray drying process with the induction of nanoscale Kirkendall diffusion. The nickel sulfide/rGO composite powders selected as the first target material exhibited excellent cycling and rate performances for Na-ion storage as anode materials for NIBs. The hollow structure of the nickel sulfide nanospheres improved the structural stability during repeated Na insertion and extraction processes. The simple sulfidation of the metal nanopowder-decorated rGO powders introduced in this study could be applied in the preparation of metal sulfide hollow nanospheres/rGO composite powders of various compositions for many applications, including energy storage.

Acknowledgements

This work was supported by the Energy Efficiency & Resources Core Technology Program of the Korea Institute of Energy Technology Evaluation and Planning (KETEP), and granted financial resource from the Ministry of Trade, Industry & Energy, Republic of Korea (201320200000420).

Notes and references

1 P. Barpanda, G. Oyama, S. I. Nishimura, S. C. Chung and A. Yamada, *Nat. Commun.*, 2014, **5**, 4358.
2 B. Dunn, H. Kamath and J. M. Tarascon, *Science*, 2011, **334**, 928.
3 H. G. Kim, J. H. Hong, K. Y. Park, H. S. Kim, S. W. Kim and K. S. Kang, *Chem. Rev.*, 2014, **114**, 11788.
4 Y. Z. Jiang, M. J. Hu, D. Zhang, T. Z. Yuan, W. P. Sun, B. Xu and M. Yan, *Nano Energy*, 2014, **5**, 60.
5 S. P. Wu, R. Y. Ge, M. J. Lu, R. Xu and Z. Zhang, *Nano Energy*, 2015, **15**, 379.
6 P. Senguttuvan, G. Rousse, V. Seznec, J. M. Tarascon and M. R. Palacín, *Chem. Mater.*, 2011, **23**, 4109.
7 D. Wu, X. Li, B. Xu, N. Twu, L. Liu and G. Ceder, *Energy Environ. Sci.*, 2015, **8**, 195.
8 S. Y. Hong, Y. J. Kim, Y. W. Park, A. Choi, N. S. Choi and K. T. Lee, *Energy Environ. Sci.*, 2013, **6**, 2067.
9 M. Gu, A. Kushima, Y. Y. Shao, J. G. Zhang, J. Liu, N. D. Browning, J. Li and C. M. Wang, *Nano Lett.*, 2013, **13**, 5203.
10 H. L. Zhu, Z. Jia, Y. C. Chen, N. Weadock, J. Y. Wan, O. Vaaland, X. G. Han, T. Li and L. B. Hu, *Nano Lett.*, 2013, **13**, 3093.
11 Y. C. Liu, N. Zhang, L. F. Jiao, Z. L. Tao and J. Chen, *Adv. Funct. Mater.*, 2015, **25**, 214.
12 K. T. Kim, C. Y. Yu, C. S. Yoon, S. J. Kim, Y. K. Sun and S. T. Myung, *Nano Energy*, 2015, **12**, 725.
13 A. Jahel, C. M. Ghimbeu, A. Darwiche, L. Vidal, S. H. Garreau, C. V. Guterl and L. Monconduit, *J. Mater. Chem. A*, 2015, **3**, 11960.
14 Y. Liu, Z. Y. Cheng, H. Sun, H. Arandiyan, J. P. Li and M. Ahmad, *J. Power Sources*, 2015, **273**, 878.
15 Z. Hu, L. Wang, K. Zhang, J. B. Wang, F. Y. Cheng, Z. L. Tao and J. Chen, *Angew. Chem., Int. Ed.*, 2014, **53**, 12794.
16 Z. Hu, Z. Q. Zhu, F. Y. Cheng, K. Zhang, J. B. Wang, C. C. Chen and J. Chen, *Energy Environ. Sci.*, 2015, **8**, 1309.
17 K. Zhang, Z. Hu, X. Liu, Z. L. Tao and J. Chen, *Adv. Mater.*, 2015, **27**, 3305.
18 Y. J. Kim, Y. I. Kim, A. Choi, S. W. Woo, D. G. Mok, N. S. Choi, Y. S. Jung, J. H. Ryu, S. M. Oh and K. T. Lee, *Adv. Mater.*, 2014, **26**, 4139.
19 J. Y. Jang, Y. W. Lee, Y. J. Kim, J. M. Lee, S. M. Lee, K. T. Lee and N. S. Choi, *J. Mater. Chem. A*, 2015, **3**, 8332.
20 Y. Y. Zhu, P. Nie, L. Shen, S. Y. Dong, Q. Sheng, H. S. Li, H. F. Luo and X. G. Zhang, *Nanoscale*, 2015, **7**, 3309.

21 D. Y. Go, J. S. Park, P. J. Noh, G. B. Cho, H. S. Ryu, T. H. Nam, H. J. Ahn and K. W. Kim, *Mater. Res. Bull.*, 2014, **58**, 190.
22 J. Yang, D. Voiry, S. J. Ahn, D. W. Kang, A. Y. Kim, M. Chhowalla and H. S. Shin, *Angew. Chem., Int. Ed.*, 2013, **52**, 13751.
23 J. Zhang, Q. Wang, L. H. Wang, X. Li and W. Huang, *Nanoscale*, 2015, **7**, 10391.
24 S. H. Choi, Y. N. Ko, J. K. Lee and Y. C. Kang, *Adv. Funct. Mater.*, 2015, **25**, 1780.
25 S. H. Choi and Y. C. Kang, *Nanoscale*, 2015, **7**, 3965.
26 S. H. Choi and Y. C. Kang, *Nanoscale*, 2015, **7**, 6230.
27 C. Q. Shang, S. M. Dong, S. L. Zhang, P. Hu, C. J. Zhang and G. L. Cui, *Electrochem. Commun.*, 2015, **50**, 24.
28 Q. Pan, J. Xie, T. J. Zhu, G. S. Cao, X. B. Zhao and S. C. Zhang, *Inorg. Chem.*, 2014, **53**, 3511.
29 J. J. Wang, C. Luo, T. Gao, A. Langrock, A. C. Mignerey and C. S. Wang, *Small*, 2015, **11**, 473.
30 J. Liu, *Nat. Nanotechnol.*, 2014, **9**, 739.
31 X. L. Li, W. Qi, D. H. Mei, M. L. Sushko, I. Aksay and J. Liu, *Adv. Mater.*, 2012, **24**, 5136.
32 Y. W. Zhu, S. T. Murali, W. W. Cai, X. S. Li, J. W. Suk, J. R. Potts and R. S. Ruoff, *Adv. Mater.*, 2010, **22**, 3906.
33 S. Han, D. Q. Wu, S. Li, F. Zhang and X. L. Feng, *Adv. Mater.*, 2014, **26**, 849.
34 W. Ai, J. Jiang, J. H. Zhu, Z. X. Fan, Y. L. Wang, H. Zhang, W. Huang and T. Yu, *Adv. Energy Mater.*, 2015, 1500559.
35 Y. C. Qiu, K. Y. Yan, S. H. Yang, L. M. Jin, H. Deng and W. Li, *ACS Nano*, 2010, **4**, 6515.
36 J. Zhang, Q. Wang, L. H. Wang, X. Li and W. Huang, *Nanoscale*, 2015, **7**, 10391.
37 X. B. Li, S. W. Yang, J. Sun, P. He, X. Xu and G. Q. Ding, *Carbon*, 2014, **78**, 38.
38 L. Ke, W. Lv, F. Y. Su, Y. B. He, C. H. You, B. H. Li, Z. J. Li, Q. H. Yang and F. Y. Kang, *Carbon*, 2015, **92**, 311.
39 J. S. Cho, Y. J. Hong and Y. C. Kang, *ACS Nano*, 2015, **9**, 4026.
40 J. S. Cho and Y. C. Kang, *Small*, 2015, DOI: 10.1002/smll.201500940.
41 L. Hu, N. Yan, Q. W. Chen, P. Zhang, H. Zhong, X. R. Zheng, Y. Li and X. Y. Hu, *Chem. – Eur. J.*, 2012, **18**, 8971.
42 Y. M. Lee, M. R. Jo, K. S. Song, K. M. Nam, J. T. Park and Y. M. Kang, *ACS Appl. Mater. Interfaces*, 2012, **4**, 3459.
43 Y. D. Yin, C. K. Erdonmez, A. Cabot, S. Hughes and A. P. Alivisatos, *Adv. Funct. Mater.*, 2006, **16**, 1389.
44 C. W. Lee, S. D. Seo, H. K. Park, S. B. Park, H. J. Song, D. W. Kim and K. S. Hong, *Nanoscale*, 2015, **7**, 2790.
45 W. Zhou, J. L. Zheng, Y. H. Yue and L. Guo, *Nano Energy*, 2015, **11**, 428.
46 Y. L. Zhou, D. Yan, H. Y. Xu, J. K. Feng, X. L. Jiang, J. Yue, J. Yang and Y. T. Qian, *Nano Energy*, 2015, **12**, 528.
47 W. J. Zhou, X. J. Wu, X. H. Cao, X. Huang, C. L. Tan, J. Tian, H. Liu, J. Y. Wang and H. Zhang, *Energy Environ. Sci.*, 2013, **6**, 2921.
48 J. L. Zhu, Y. Y. Li, S. Kang, X. L. Wei and P. K. Shen, *J. Mater. Chem. A*, 2014, **2**, 3142.
49 J. W. Xiao, L. Wan, S. Yang, F. Xiao and S. Wang, *Nano Lett.*, 2014, **14**, 831.
50 H. C. Chen, J. J. Jiang, L. Zhang, H. Z. Wan, T. Qi and D. D. Xia, *Nanoscale*, 2013, **5**, 8879.
51 U. N. Maiti, J. W. Lim, K. E. Lee, W. J. Lee and S. O. Kim, *Adv. Mater.*, 2014, **26**, 615.
52 B. Guo, X. Wang, P. F. Fulvio, M. Chi, S. M. Mahurin, X. G. Sun and S. Dai, *Adv. Mater.*, 2011, **23**, 4661.